

Improving local and global mechanical properties of friction stir welded thick AA7075-T6 joints by optimizing pin-tip profile

Yuqing Mao¹ · Liming Ke^{1,2} · Yuhua Chen² · Fencheng Liu² · Li Xing²

Received: 1 February 2016 / Accepted: 9 May 2016 / Published online: 25 May 2016
© Springer-Verlag London 2016

Abstract Four tools with taper (TA), triangular (TB), three-grooves (TC), and square (TD) pin-tip profiles were designed to friction stir weld (FSW) thick AA7075-T6 alloy plates aiming at improving the local and overall mechanical properties of the joints. The microstructure evolution, hardness, and mechanical properties of the FSW joints were studied by scanning electron microscope (SEM), X-ray diffractometer (XRD), and transmission electron microscope (TEM). The results show that equiaxed grains in the bottom nugget zone (BNZ) obtained by using TC are noticeably refined compared to in the case of other tools. Also, finer and more dispersive precipitates are distributed in this BNZ, and higher contents of η phase and dislocations are observed. A similar trend is found in the middle of weld. The bottom slices welded by employing TC show superior strength and ductility with a highest ultimate tensile strength of 388 MPa, yield strength of 315 MPa, and elongation of 7.9 %, which are in agreement with the hardness profiles. This is owing to ultrafine grains, more high-angle grain boundaries, more dispersive and higher contents of precipitates, and optimum hardness distribution. Accordingly, the global mechanical properties of the overall joints prepared by using TC significantly improve.

Keywords Friction stir welding · Pin-tip profile · AA7075-T6 alloy · Thick plates · Microstructure · Mechanical properties

1 Introduction

High-strength 7xxx series aluminum alloys are widely used in the aircraft, aerospace, and other engineering applications due to their high strength to weight ratio, fracture toughness, excellent corrosion resistance, and natural aging characteristics [1–3]. Similar to 2xxx series aluminum alloys, 7xxx series alloys, such as AA7075 and AA7050, are considered relatively difficult to weld using fusion welding processes because of the presence of copper which will result in loss of strength and ductility in the heat-affected zone, leading to brittle fracture, hot cracking, porosities, and fusion defects [4, 5]. Although it is possible to avoid solidification cracks by using a proper heat-treatable aluminum alloy filler, the resulted joint efficiencies are unsatisfactorily low [6]. AA7075 is a high-strength alloy complying with Al-Zn-Mg-Cu system of 7xxx series alloys. It gains strength from main $MgZn_2$ precipitates and is suitable for military and aircraft structural components because it can recover strength from the natural aging after welding [7]. But, the applications of AA7075 alloy are currently limited because of many problems during welding.

Friction stir welding (FSW) is a solid-state joining process in which the material to be welded does not melt and recast. Thus, this technique is well suited to weld aluminum alloys, especially those which are normally considered to be unweldable, such as 7xxx series aluminum alloys. It may avoid the weld defects like cracks and porosities, significantly improving mechanical properties of the joints [8]. During FSW, a nonconsumable rotating tool, including a special shoulder and pin, moves forward along the joint interface to generate heat, leading to a recirculating flow of plasticized

✉ Liming Ke
liming_ke@126.com

¹ State Key Laboratory of Solidification Processing, Northwestern Polytechnical University, Xi'an 710072, People's Republic of China

² National Defence Key Discipline Laboratory of Light Alloy Processing Science and Technology, Nanchang Hangkong University, Nanchang 330063, People's Republic of China

material around the tool surface. The softened material underneath the shoulder is subjected to extruding by the tool pin in rotational and traverse movements which transport from the advancing side to retreating side where it is joined into a weld [9, 10].

A large number of research papers are reported on the FSW of aluminum alloy sheets, introducing the material flow [11, 12], microstructure evolution [13], mechanical properties [14], fatigue [15], and corrosion behaviors [16]. However, it is observed that few papers exist about the FSW of precipitation-hardening AA7075. Especially for thick plates, lots of welding problems still remain. Avettand Fenoel and Taillard [17] demonstrated that the nugget hardness decreased along the weld thickness direction due to the temperature gradient and deformation, which resulted in heterogeneous nugget microstructures in 19-mm-thick FSW welds of AA2050. Also, Canaday et al. [18] proved that the nugget hardness near the weld root was less than one at the midplane and near the crown for friction stir welding of 32-mm-thick AA7050 alloy plates, indicating that the peak temperature in the root was lower than that in the midplane and crown. Srinivasa Rao et al. [19] found that the FSW joint efficiency in thick plates was only 53 % for 16 mm welds and 70 % for 10 mm welds with compared to 80–90 % for 3–6-mm sheets of the same material, which was mainly due to the higher heat input. Xu et al. [20] reported that the strength and elongation decreased significantly from the top to the bottom of the weld along the thickness for FSW of 14-mm-thick AA2219 alloy plates. A lowest temperature was found in the weld root. Based on the results from the abovementioned papers, it can be concluded that low temperature and poor plastic flow in the weld root result in the performance deterioration at the root and also reduce the overall mechanical properties of the FSW joints of thick plates. Therefore, how to improve the flowability of plastic material in the weld root will be focused on in this study.

It is well known that the formation characteristics of the FSW joints are influenced by material flow and temperature distribution across the weld, which are determined by tool geometries and welding parameters [21, 22]. The tool geometry, in particular the pin profile, is a predominant factor in determining the weld geometry, localized heating, and stirring action. Besides, it predominantly governs the flow path of plastic material around the pin and is responsible for homogeneous microstructure, and uniform joint properties [23]. Thomas et al. [24] declared that Whorl™ and MX Triflute™ tool geometries increased heat generation and lowered displacement volumes of the softened materials during FSW. Analogously, Zhang et al. [25] revealed that the tool with three-sided pin profile increased its stirring power and hence promoted the metal flow under the probe end due to higher surface velocity at the probe edge. Meanwhile, Thomas and Nicholas [26] found that the eccentricity allowed

incompressible material to pass around the pin profile due to dynamic orbit with relative eccentricity. Elongovan and Balasubramanian [27] showed that pin profiles with square and triangular flat faces were associated with this eccentricity. In addition, the triangular and square pin profiles produced a pulsating stirring action in the flowing material due to flat faces, while there was no such pulsating action in the case of tapered and threaded pin profiles. Dawood et al. [28] studied that the FSW joints of AA6061 alloy had the best mechanical properties by using the triangular tool pin profile compared with threaded tapered and square pins. Less pulsating action experienced in the nugget zone (NZ) of triangular pin, leading to formation of finer grains. However, Khodaverdizadeh et al. [29] reported that square pin profile caused higher degree of plastic deformation due to its higher eccentricity and pulsation effect, and also led to higher peak temperature as well as finer recrystallized grains in the FSW joints of 5-mm-thick copper plates. Hence, based on the reasons mentioned above, the results are summarized as a baseline for the present study. The aim of this paper is to improve the local plastic flow and temperature distribution in the bottom of weld in order to improve the weld properties. For this purpose, four different tool pin-tip profiles (threaded taper, triangular, three-grooves, and square pins) are selected to weld thick aluminum alloy plates under the same welding parameters. The microstructure and mechanical properties of the achieved joints are investigated.

2 Experimental procedures

Twenty-millimeter-thick AA7075-T6 aluminum alloy rolled plates were used as base material (BM) in the study. Chemical compositions and mechanical properties of this alloy are illustrated in Table 1. Plates were cut into a required size of 200 mm (length) × 140 mm (width) × 20 mm (thickness), and then joined by FSW perpendicular to the rolling direction. A modified horizontal-type milling machine was used. Four different tools with taper, triangular, three-groove, and square pin-tip profiles coupled with the same left thread were designed to fabricate the joints. The schematic diagram is shown in Fig. 1. The tool handle and shoulder were made of H13 die steel. The pin material was GH4169 steel. The tool sizes were both having 14 mm in pin root diameter, 8 mm in the head, 19.5 mm in total length, and 3 mm in tip height, as well as a concave shoulder of 42 mm in diameter. The thread pitch was 2 mm. Constant tool rotation speed of 475 rpm and welding speed of 37.5 mm/min were applied by trial and error. Moreover, a spindle tilt angle of 2° and a plunge depth of 0.5 mm were used during FSW.

The microstructural features of the joints were examined by electron backscattering diffraction (EBSD), scanning electron microscope (SEM), and transmission electron microscope

Table 1 Chemical composition and mechanical properties of 7075-T6 aluminum alloy

Chemical composition (wt.%)								Mechanical properties			
Zn	Mg	Cu	Si	Fe	Mn	Cr	Al	σ_b (MPa)	$\sigma_{0.2}$ (MPa)	A (%)	Hardness (HV)
5.81	2.68	1.66	0.35	0.61	0.33	0.2	Bal.	535	470	8.7	160–170

(TEM). The EBSD samples (marked by red boxes in Fig. 2) were cut from the FSW joints transverse to the welding direction. After standard grinding and mechanical polishing procedures, an electrochemical compound polishing with a solution of 8 % perchloric acid alcohol for 15 s at -20 °C with an applied potential of 20 V was conducted. EBSD studies were performed in a TESCAN VEGA II-LMH SEM with step size of 0.5 μm for data collection. The TEM samples were prepared by twin-jet electro-polish in a solution of 25 vol.% of HNO_3 and 75 vol.% of methanol at a temperature of -30 °C, and then observed by TEM which was operating at 200 keV. The voltage was set as 12 V. The phase composites and types were analyzed by X-ray diffraction (XRD) with $\text{Cu K}\alpha$ radiation on D8X diffractometer. The XRD samples with a size of 2 mm (length) \times 2 mm (width) \times 3 mm (thickness) were cut from the weld nugget center and polished, and then were tested for different samples, respectively.

Vickers hardness was measured on the middle and bottom cross sections of the joints perpendicular to the welding direction. The interval between two points was 1.0 mm, as shown in Fig. 2. A load of 100 g and a dwell time of 10 s were selected for hardness testing. The tensile specimens including the bottom slices of 5 mm in thickness (δ_1) and overall joints of 20 mm (δ_2) in thickness were prepared as per the ASTM: B557M-10. The dimensions of tensile specimens (bottom slice and whole) are shown in Fig. 3. The specimen surface and edge were rounded and polished during the tensile tests to avoid

the surface stress concentration. The room temperature tensile tests were conducted at a cross-head speed of 1 mm/min using a WDS-100 universal testing machine. The tensile properties of each joint were evaluated using three tensile specimens machined from the same joint. After the tensile test, the fracture features of the samples were analyzed by SEM.

3 Results and discussion

3.1 Microstructure

Figure 4 shows the microstructural characteristics observed by EBSD in the bottom nugget zones (BNZs) of the joints (region A in Fig. 2) welded by different tools of TA, TB, TC, and TD, respectively. Microstructure in NZs is known to exhibit a typical feature of fine and equiaxed grains due to dynamic recrystallization which attributes to the highest plastic deformation and peak temperature. The recrystallization is a complex nucleation and growth process described as follows: (1) at the initial stage, the substrate turns into coarse band structures. As the strain increases, some elongated fibrous grains are formed, and then a finer scale is obtained as further grain subdivision continuously occurs. (2) With an increase in temperature, fine nugget-scale grains are formed from closely spaced parallel high-angle grain boundaries (HAGBs). The bands of fine grains are forced together and increased in volume fraction with strain. (3) The unstable fibrous grain fragments form a full nugget-like microstructure consisting of low aspect ratio ultrafine grains, and finally grow up to more equiaxed structures due to static annealing in the thermal wake of the tool [30, 31]. The growth is accomplished mainly by the migration of HAGBs. However, various recrystallization mechanisms during FSW have been reported, such as dynamic recovery

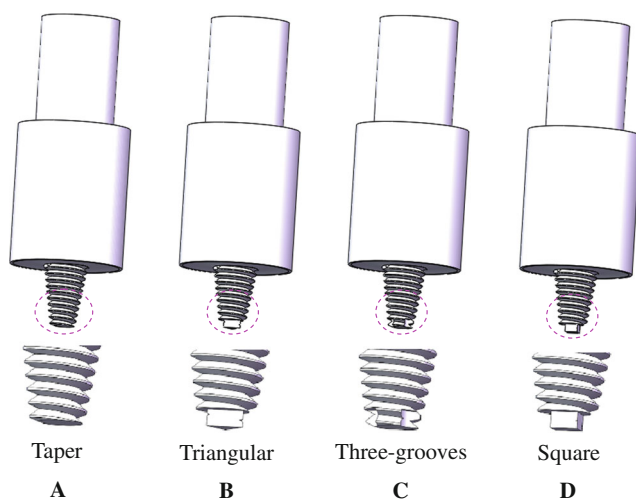


Fig. 1 Schematic diagrams of tool pin designs used (marked for TA, TB, TC, and TD, respectively)

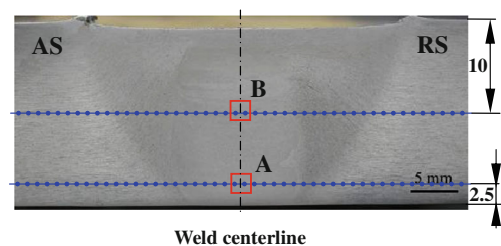
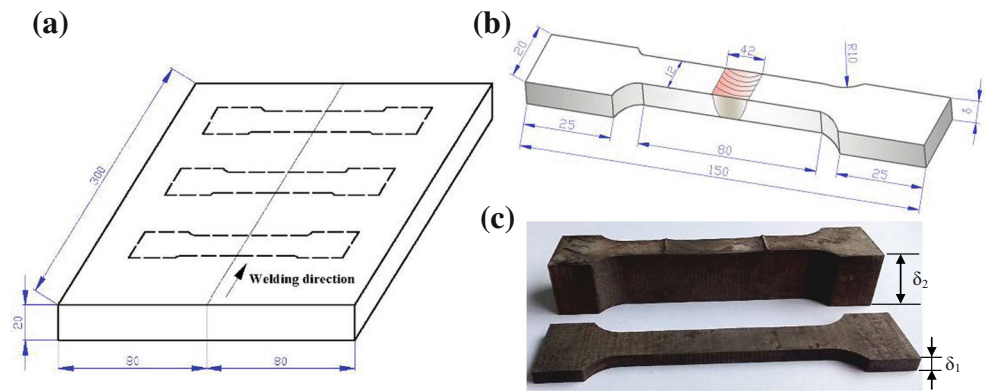


Fig. 2 Macromorphology of the weld for showing hardness measuring and microstructure observation points

Fig. 3 Schematic illustration of tensile test specimens



(DRV), continuous dynamic recrystallization (CDR), discontinuous dynamic recrystallization (DDR), and particle nucleation, which decide the recrystallized grain in size [2, 32]. As is shown in Fig. 4, all four BNZs are composed of ultrafine grains with typical recrystallized equiaxed microstructures. But, it is clear that the grain sizes estimated by EBSD are different, which are 10.8 ± 1.2 , 7.7 ± 0.8 , 3.0 ± 0.3 , and 4.7 ± 0.5 μm for the BNZs obtained using TA, TB, TC, and TD, respectively, as shown in Fig. 5. The grains are obviously refined in different degrees with compared to those in the joints welded using TA. The grains size obtained by TC (three-groove pin-tip profile) is the smallest.

It is believed that most of the heat in FSW is determined by shoulder design. Therefore, for the same shoulder, the tool pin does not have a significant effect on the total heat generation rate during FSW. Only the way in which heat is generated by friction of deformation varies with the pin profile which plays a crucial role in the material flow path and the degree of plastic deformation [13, 21, 27, 31]. The tool with three-groove pin profile has a stronger stirring power and hence promotes the localized heating and metal flow under the probe end due to a higher surface velocity at the probe edge [23–25]. In addition, triangular and square pin profiles produce eccentricity that is defined as the ratio of the dynamic volume swept by the tool to the static volume of the tool. Triangular pin profile, with higher eccentricity, allows more incompressible materials to pass around the pin profile. Compared with triangular pin profile, the square pin profile can produce more intense

pulsating stirring action for the flowing material due to the associated eccentricity, which generates additional friction heat resulting in a higher localized plastic deformation at the tool pin and workpiece interface [26–29]. However, triangular and square pins have smaller interfacial contact areas with workpiece that reduce heat generation and degree of deformation during FSW. In contrast, the three-groove pin profile, having the strongest stirring power and the biggest contact area with the weld metal, can result in the highest plastic degree and most frictional heat to promote the peak temperature and plastic flow in the weld root in four tools, leading to finer grains, as shown in Fig. 4c. For the taper pin profile, it is ineffective to produce pulsating stirring action. The material flowability at the weld root is very poor due to lacking of sufficient stirring power. Correspondingly, the grains are coarser shown in Fig. 4a.

Using the misorientation angle distribution derived from EBSD maps shown in Fig. 4, the grain reorientation during FSW can be further understood. Figure 6 shows the misorientation angle distribution histograms of point A in Fig. 2 corresponding to the BNZs of different samples obtained by TA, TB, TC, and TD, respectively. It is obvious that the frequencies of the misorientation angles appear to have random distributions. Moreover, considering all grain boundary misorientation angles $>2^\circ$, the HAGBs in the BNZs produced by TC contribute much more than other tools. It can be concluded that a much higher fraction of HAGBs exists in the BNZ due to a more dynamic recrystallization. It is proved that HAGBs

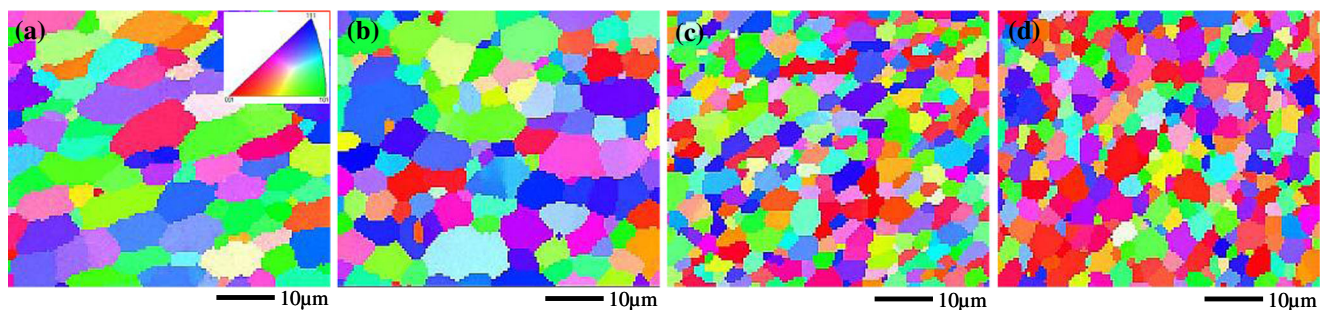


Fig. 4 EBSD maps at 2.5 mm from the bottom surface of NZ for the joints obtained by (a) TA, (b) TB, (c) TC, and (d) TD, respectively

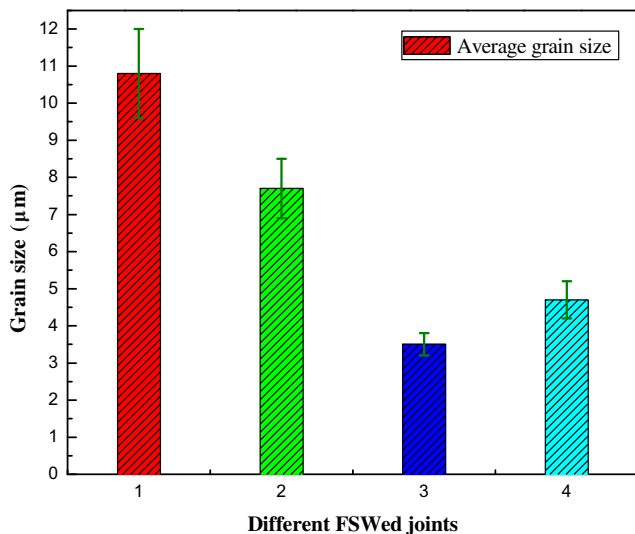


Fig. 5 Average grain size in the BNZs of the different joints

can efficiently hinder the dislocations and thus improve the strain hardening capacity and the ductility. Also, reasonable ductility could be obtained by HAGB sliding and related activities in ultrafine grain materials. The main attribution is that

HAGB sliding may lead to dislocation emissions at triple junctions due to high stress concentrations, and those dislocations hence the strain hardening [33, 34].

In order to further analyze and discuss the effect of pin-tip profiles, the microstructures in the middle of the FSW joints (region B in Fig. 2) are shown in Fig. 7. It is seen that there is a difference in the grain size. The one obtained by TC is smaller than other tools. The reason may be related to plastic flow and peak temperature mentioned from the above description.

3.2 Precipitates distribution and XRD analysis

Figure 8 shows TEM images in the bottom of NZs of the joints produced by four different pin-tip profiles. The material within the BNZs experiences intensive plastic deformation and high temperature, and the microstructure evolution occurs continuously. The peak temperature in the BNZs is in a range of 400–510 °C for the FSW of AA7075 alloy as reported in [35]. Most of the coarse secondary phase particles in BM are broken up, dissolved, and reprecipitated during FSW. Fine reprecipitated phases are distributed in the BNZs. In addition, it is obvious that the precipitate distributions in the BNZs are

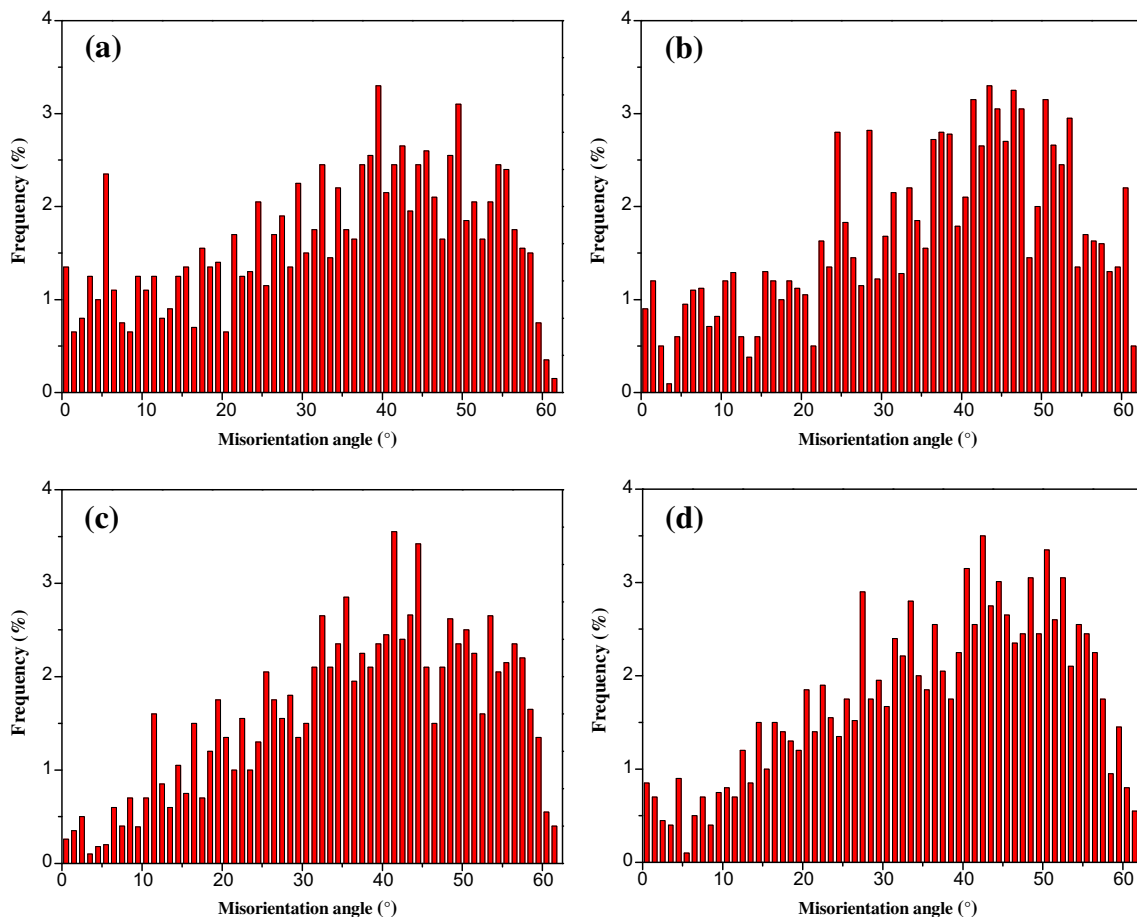


Fig. 6 Misorientation angle distribution in BNZs of the joints obtained by (a) TA, (b) TB, (c) TC, and (d) TD, respectively

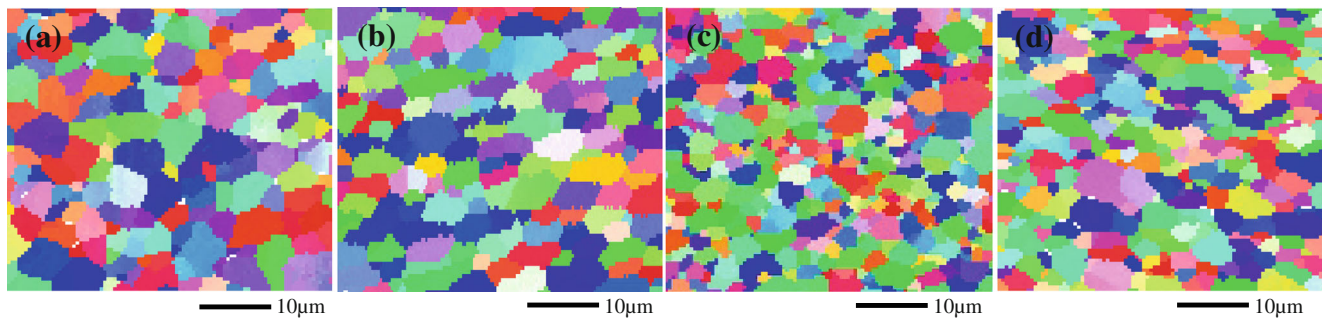


Fig. 7 Microstructure of the middle at 10 mm from the top surface in different NZs under (a) TA, (b) TB, (c) TC, and (d) TD, respectively

different. The strengthening particle distribution in the BNZ obtained by TA is very inhomogeneous and random and is composed of fine reprecipitated phases as well as some coarse unbroken particles due to inadequate stirring action of the pin for the local bottom region, as shown in Fig. 8a. By EDX microanalysis, these dispersoids are mainly identified as η phase (MgZn_2), S phase (Al_2CuMg), and T phase (AlMgZnCu), respectively. However, the precipitate distributions in other BNZs are relatively uniform, especially for the sample welded by TC. These particles are η phase (MgZn_2) as indentified by EDS shown in Fig. 8c. It is well known that fine η phase in the weld plays an important role in hindering abnormal grain growth and is effective in dislocation pinning and accumulation. For the FSW of precipitation strengthening aluminum alloy, the precipitate distribution is intensively

studied [1, 7, 9, 31]. Canaday et al. [18] found that the weld properties in the root became noticeably worse due to coarse precipitates resulting from a lower temperature for FSW of 32-mm-thick AA7050 plates. Mao et al. [31] proved that the precipitated particles in the weld bottom were coarser and badly nonuniform than those in the top/middle for FSW of thick AA7075 alloy plates. Similarly, Xu et al. [20] reported that the strengthening particle size in the weld bottom was larger in FSW of thick AA2219 alloy plates, significantly decreasing the hardness and tensile property of the joints. Also, the high-resolution TEM images of the coarse and fine η phases observed in this study are shown in Fig. 8e, f, respectively. During FSW, although the material in the weld undergoes large plastic deformation and high temperature, some dislocations with a high density which are caused by the

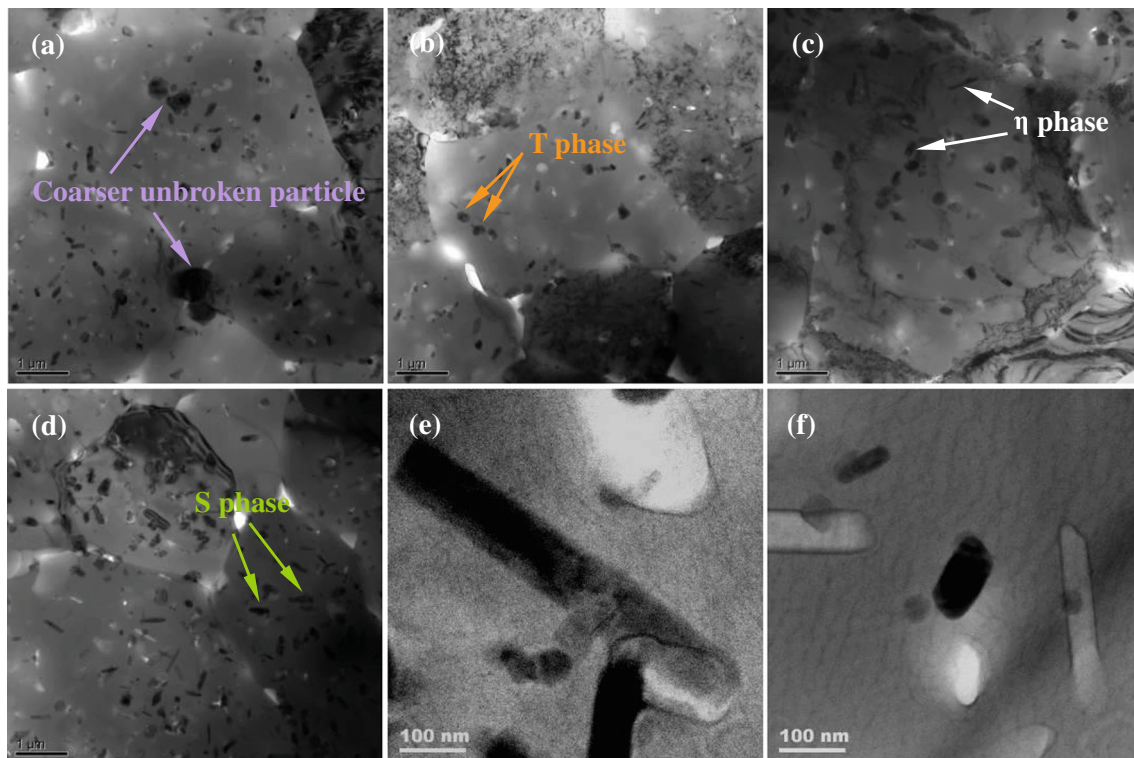


Fig. 8 TEM micrographs showing the precipitates at 2.5 mm from the bottom surface of the NZs obtained by (a) TA, (b) TB, (c) TC, and (d) TD, respectively; HRTEM in [100] zone axis showing e coarse and f fine η (MgZn_2) phases

dynamic recrystallization are left in the BNZ after welding shown in Fig. 8b, c. These dislocations can pile up against the precipitated particles and serve as the nucleation sites for the η phase during artificial aging for 7xxx aluminum alloy. Moreover, a high density of dislocations is conducive to improve the mechanical properties of the joints. Similar results such as dislocation pinning effects are observed and proved in FSW of AA7050-T7451 alloy [2], AA2024 alloy [36], and AA6061-T651 alloy [37].

In order to estimate the content of the precipitated phases in the BNZs for different tools, the XRD experiment is used in this research. XRD profiles including all precipitate distributions and MgZn_2 phase diffraction peak are shown in Fig. 9a, b, respectively. As shown in Fig. 9a, it is clear that three types of strengthening phases, including η phase, T phase, and S phase are examined, which is consistent with the TEM results shown in Fig. 8. However, there is an apparent difference in the precipitate content. For example, the diffraction peak of η phase is higher with compared to other phases in the same BNZ, but only few T and S phases are found, indicating that the reprecipitated particles is almost single phase, i.e., η phase (MgZn_2), after welding. In the 7xxx series aluminum alloys, the supersaturated solid-solution is decomposed in the following sequence: supersaturated solid-solution \rightarrow GP zone \rightarrow η (MgZn_2) \rightarrow η (MgZn_2). Decomposition of the supersaturated solid-solution produces solute-rich clusters, GP (I), and vacancy-rich clusters which will transform or nucleate into GP (II) zones. Both types of GP zone can form at a low temperature of 20–125 °C, but the GP (I) zone dissolves at a lower temperature of 100 °C than the GP (II) at 125 °C. At higher aging temperatures from 130 to 290 °C, the formation of the metastable and semicoherent η phase is followed by formation of the equilibrium η phase. Both of these phases are hexagonal with different lattice parameters. Furthermore, the equilibrium η phase forms directly from solid-solution [2, 31, 32]. Figure 9b shows the diffraction peak of η phase in different BNZs. It is deduced that BNZ obtained by TC has more MgZn_2 phase. One reasonable interpretation is that the tool with three-groove pin profile can result in higher temperature which is beneficial to sufficient solid solution and reprecipitation of the strengthening phases during FSW. In this FSW process using TC, other phases are barely formed but it is followed by the precipitation sequence shown above. Hence, it can be deduced that finer and more precipitated particles are helpful to improve the local mechanical properties of the weld bottom by optimizing pin-tip profile.

Figure 10 shows SEM images of strengthening particles in the middle of weld for different joints fabricated by TA, TB, TC, and TD, respectively. EDS analysis reveals that the white particles distributed dispersively in Al substrate are η phase of AA7075 alloy together with few gray particles containing Al, Mg, Zn, and Cu. However, as shown in Fig. 10, there is a difference in precipitate sizes. The precipitated particles

shown in Fig. 10a are coarser and distributed at random for TA. Compared to Fig. 10a, b, d, the middle of weld obtained by TC shows finer grains with homogeneously dispersed particles as shown in Fig. 10c. This is mainly due to a higher temperature and better plastic flow in the weld stemming from stronger stirring action of the tool pin, which causes finer and more uniform precipitates in the middle. Mironov et al. [38] suggested that the tool pin played a main role in governing the formation quality and microstructure by influencing the flow behavior in the weld. Intense stirring effect for plasticized material was beneficial to form finer microstructures. In addition, it should be noted that the grain refinement in the weld is associated with the resistance of dispersed particles to grain growth in the dynamic recrystallization during FSW [2, 32], which is reflected by the microstructures in Fig. 7.

3.3 Mechanical properties

3.3.1 Microhardness

For FSW of 7xxx series alloys, the hardness variation accurately corresponds to the change in microstructure, which is usually used to analyze the mechanical properties of the joints. Figure 11 shows the Vickers microhardness profiles transverse to the cross section at two horizontal locations. The BM (AA7075-T6 alloy) exhibits microhardness values in a range of 160–170 HV. In Fig. 11a, it is clear that the hardness distribution across the weld nugget zone (WNZ) and adjacent regions shows a W shape, and a softening phenomenon is presented in the thermal-mechanically affected zone (TMAZ) and heat-affected zone (HAZ) compared with the WNZ and BM. It is mainly attributed to two factors. First, the grains and strengthening phases are obviously coarsened in the TMAZ and HAZ. Second, GP zones are completely or partially dissolved due to thermal cycle during FSW. Similar results were reported in [39, 40]. Compared with other joints, the microhardness values are higher in the BNZ of the joint produced by TC. According to the Hall–Petch relationship ($H_V = H_0 + k_H d^{-1/2}$, H_V is the hardness, d is the grain size, H_0 and k_H are the contents) [41], there is a great attribution to increase the hardness of the joint due to smaller grain sizes as shown in Fig. 4c and a higher fraction of HAGBs resulting in strain hardening as shown in Fig. 6c. And finer and more precipitated particles are found in the BNZ shown in Figs. 8c and 9c, respectively, which is also beneficial to enhance the hardness too. Similar results were observed in AA2024 alloy in [36, 40], where the hardness profile greatly depended on the grain size and particle distribution. Moreover, the hardness profile shows an asymmetrical distribution, and the hardness values on the AS are higher than those on the RS. The main reasons are that better shear strain and plastic flow on the AS lead to finer microstructures and more efficient strain hardening.

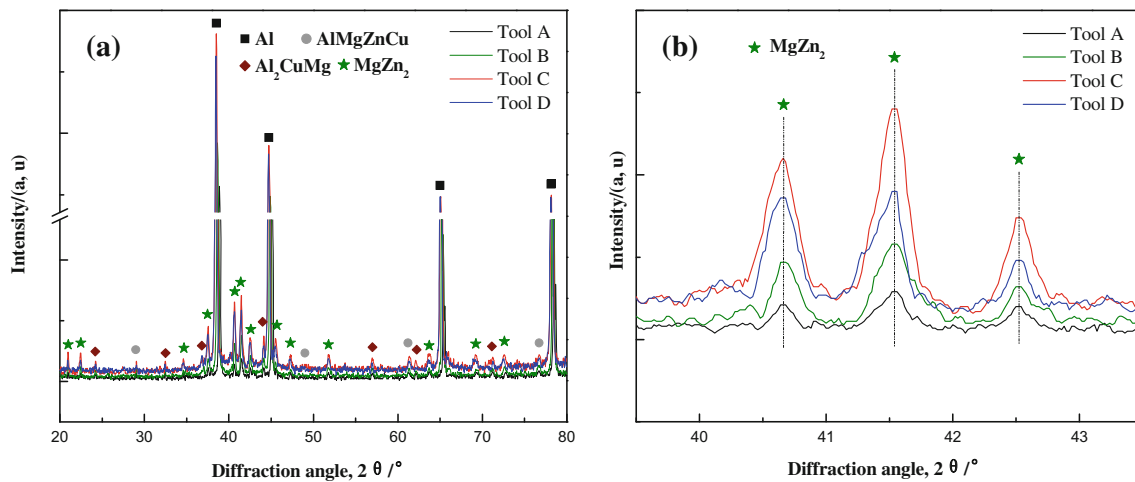


Fig. 9 XRD profiles of precipitated phases in the BNZs: **a** all the phase distributions, **b** MgZn₂ phase diffraction peak

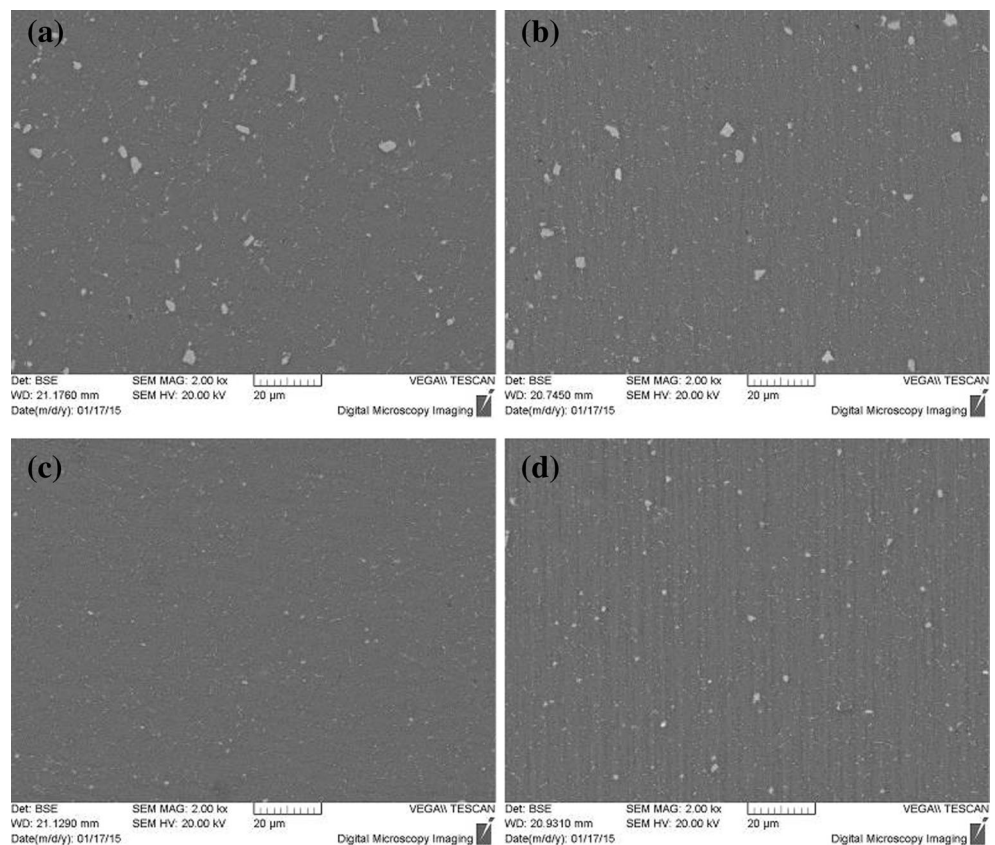
Figure 11b shows the hardness distribution in the middle of the joints. Some similar trends are displayed. The hardness of the joint made by TC is significantly higher than other joints, and its distribution on two sides is asymmetric. These phenomena are also well understood by observing the grain structures and particle distributions, as shown in Figs. 7 and 10, respectively. In a word, optimum hardness distribution was obtained in the middle and bottom of the joints produced by TC. The higher hardness will significantly decrease the formation and growth rate of microcracks, and thus improve the

local and overall mechanical properties like the ductility and strength of the joints.

3.3.2 Tensile property

In order to evaluate the effects of pin-tip profiles on mechanical properties, the tensile tests of the bottom slice and overall joint containing the nugget zone at the center are carried out. Figure 12a shows the true tensile stress–strain curves of the local bottom slices for different pin-tip

Fig. 10 SEM micrographs showing secondary phase particle distribution of the middle at 10 mm from the top surface under **a** TA, **b** TB, **c** TC, and **d** TD, respectively



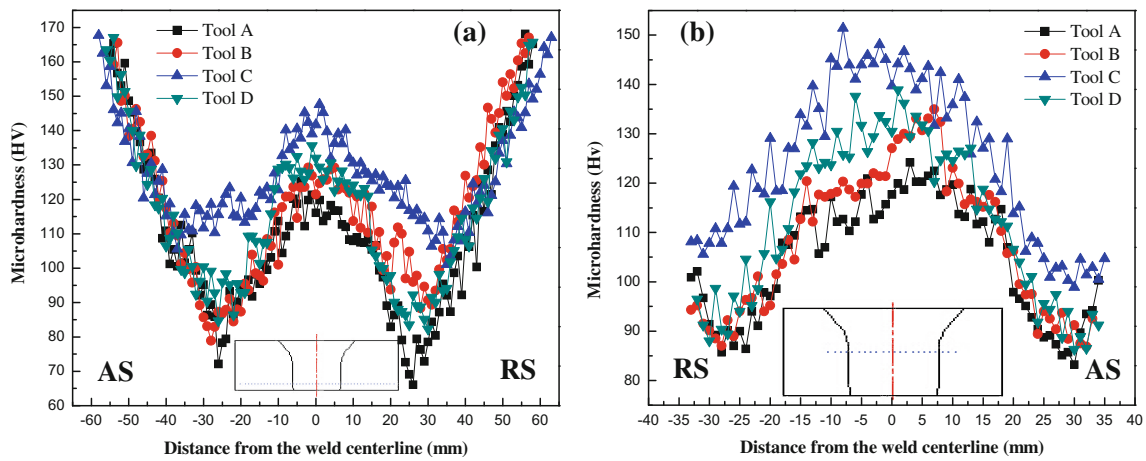


Fig. 11 Microhardness of the weld in different positions: **a** the weld bottom; **b** the middle

profiles, and Fig. 12b reveals the results of BM and overall joints. The results including the strength and elongation of the tensile samples are presented and compared in Fig. 12c, d, respectively. Error bars in Fig. 12d indicate the total range of test results for three specimens per condition. It can be clearly seen from Fig. 12c, d that the ultimate tensile strength (UTS), yield strength (YS), and

ductility of the bottom slices and overall joints under different conditions are less than the BM due to the thermal history during FSW. Moreover, it is found that the lowest UTS of 238 ± 2 MPa, YS of 172 ± 1.5 MPa, and elongation of 4.1 % were obtained for the bottom slices welded by TA. There is a significant increase in the mechanical property for using TC. The bottom slices have the highest

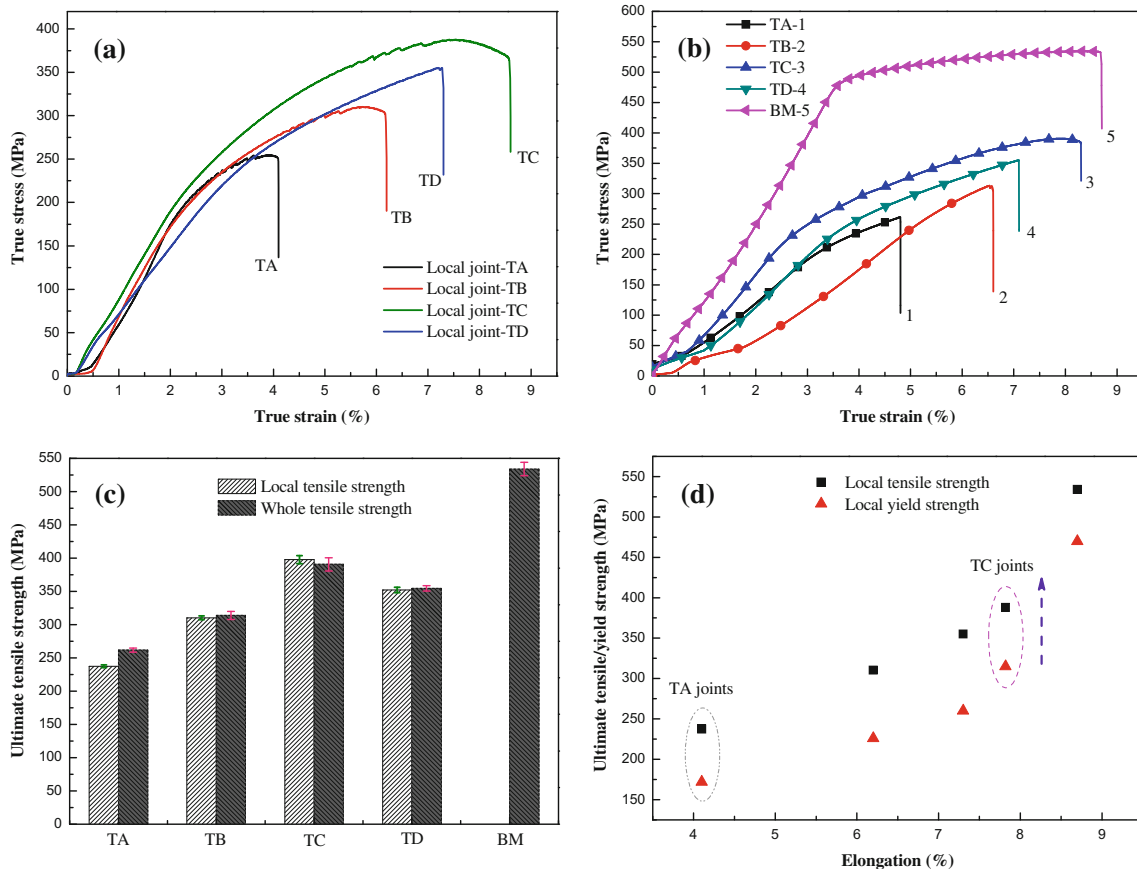


Fig. 12 Mechanical properties of the local and whole joints: **a** stress–strain curves of the bottom slices, **b** stress–strain curves of the whole joints, **c** tensile strength of the bottom slices and the whole joints, and **d** strength and elongation of the slices and joints

Table 2 Effect of tool pin-tip profile on fracture properties of the local slices and overall joints





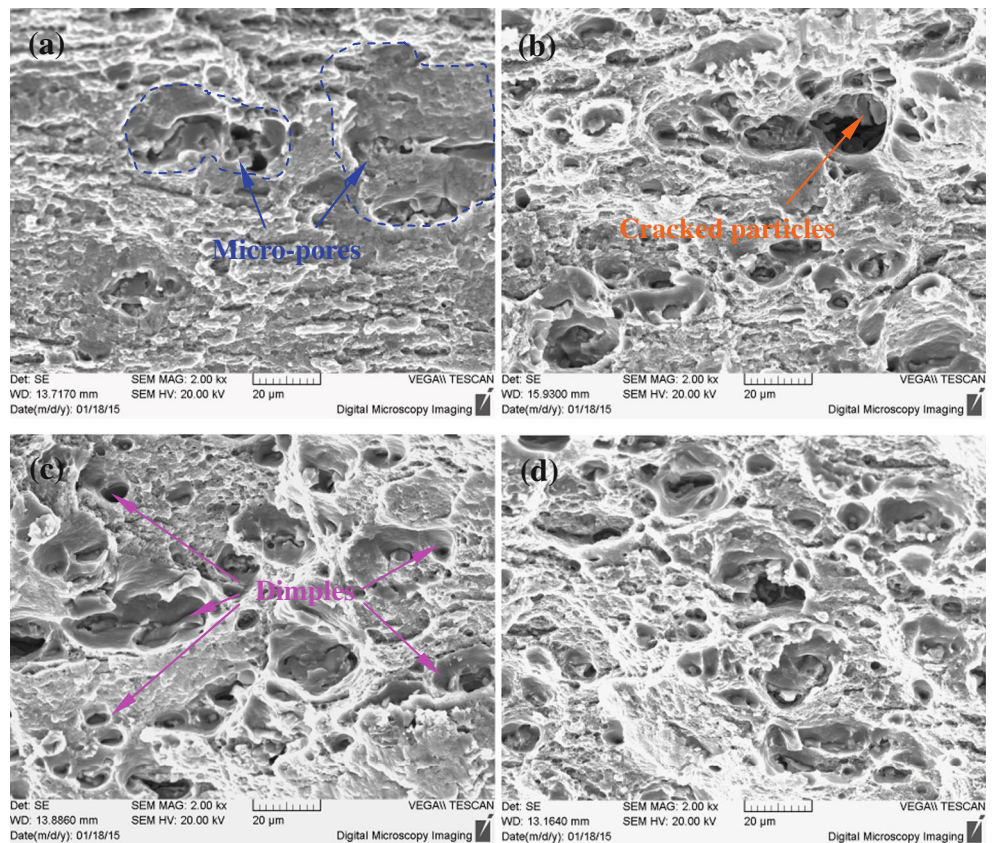
Pin-tip profile	Local bottom slice/overall joint	Minimum hardness (HV)	Fracture location	Photograph of fractured specimen
Taper (TA)	Slice	62	NZ	
	Overall	84	NZ	
Triangular (TB)	Slice	79	HAZ, AS	
	Overall	87	NZ	
Three-grooves (TC)	Slice	101	HAZ	
	Overall	103	HAZ, RS	
Square (TD)	Slice	82	HAZ, RS	
	Overall	87	NZ	

Fig. 13 SEM micrographs showing the tensile fracture surfaces of the bottom slices produced under **a** TA, **b** TB, **c** TC, and **d** TD

strength and elongation, which are 388 ± 3 MPa, 315 ± 1.5 MPa, and 7.9 %, respectively.

Primary analysis is related to the microstructure evolution and precipitated particle distribution. In general, for thick Al alloy plates welded by taper pin, the material in the bottom of weld experiences poor stirring action of the pin and lower temperature, resulting in insufficient plastic flow of the material [18–20, 31]. Thus, coarser grains, fewer strengthening particles, and fewer precipitates in the BNZ obtained by TA cause lower strength and ductility in the bottom slices, leading to the performance deterioration of the overall joints. Using the tool of TC can enhance stirring effect for the root material owing to more forceful stirring power of the pin, resulting in a better flowability of plasticized material and temperature distribution in the bottom of weld. Therefore, it is shown that all results exhibit better strengths with an increase in the elongation. The superior strength–ductility synergy with better UTS, YS, and higher elongation should be attributed to the following factors: (1) smaller grain size (in Figs. 4 and 7), (2) more HAGBs (in Fig. 6), (3) finer and more dispersive precipitated particles (in Figs. 8 and 10), (4) higher content of reprecipitated strengthening phases (in Fig. 9), and (5) optimum hardness distribution in the joint (in Fig. 11). During the tensile process, finer grains can effectively increase the distance of dislocation glide and decrease the number of dislocation pile-ups. More dispersive and uniform precipitated

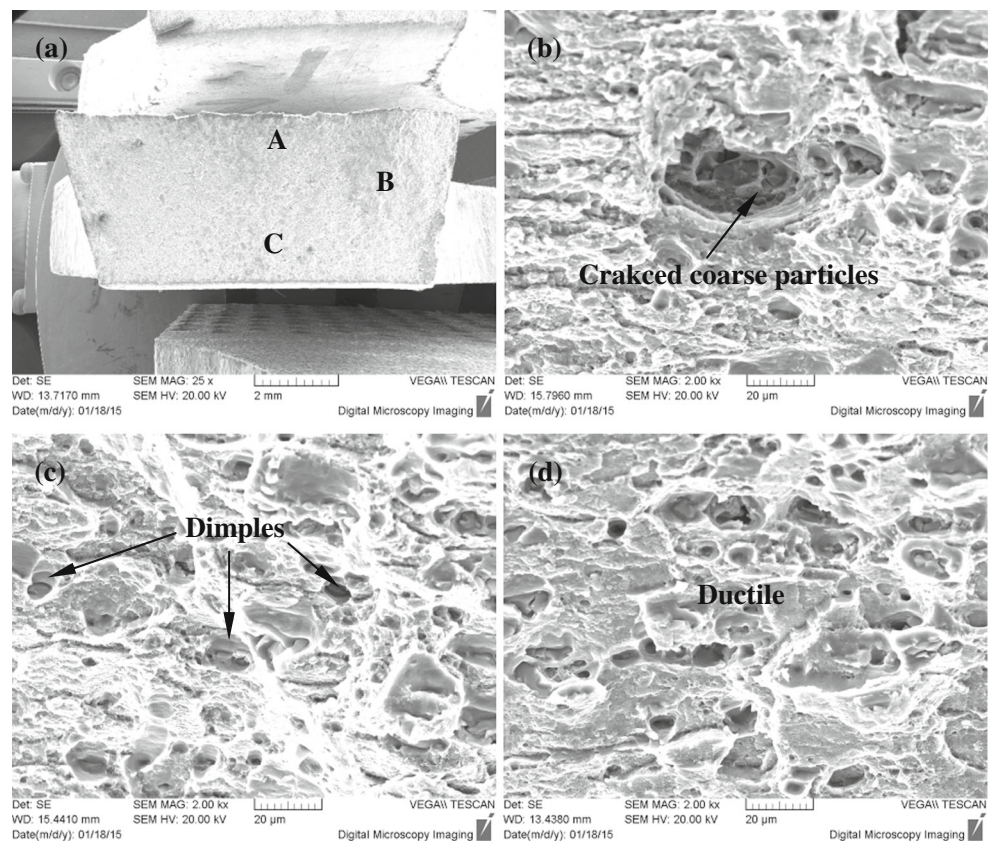
particles can impede the dislocation motion because of the pinning effect [31], which can greatly improve the mechanical properties of the joints by reducing the stress concentration as well as the formation and growth rate of microcracks.

3.4 Fracture locations and surface morphologies

For FSW of aluminum alloy plates, the microhardness distribution and presence of weld defects such as tiny pores in the joints significantly affect the tensile properties and fracture locations. In general, the fracture location occurs from the lower hardness regions of the joint that correspond to the lowest tensile strength. Table 2 presents the effect of tool pin-tip profile on fracture properties of the FSW joints. It is clear that, on a macroscopic scale, most macrofracture surfaces of the tensile-tested bottom slices present 45° shear fracture along the tensile axis in the HAZ, which are in agreement with the hardness distribution in these regions as shown in Fig. 11a. But, the bottom slices made by TA failed in the NZ. It may be caused by the presence of micropores in this region. For the overall joints, the tensile joints almost fractured in the NZ except that the failure of the samples obtained by TC occurred in the HAZ.

The fracture surfaces of the bottom slices are characterized by SEM, as shown in Fig. 13. Figure 13a shows a typical brittle fracture starting from the micropores in the joints. It

Fig. 14 SEM fractographs of the overall joints welded by TC: **a** overall morphology; **b–d** showing at high magnification of A, B, and C zone, respectively



may be concluded that a worse plastic flow occurs in the bottom of weld by using TA, and the metal does not have good metallurgical binding. Nonetheless, these joints produced by other tools reveal some transgranular fracture along with deep dimples with various sizes and shapes, and thick tear ridges full of microvoids, which is an indication that the failure is ductile, as shown in Fig. 13b–d, respectively. Obviously, it is seen from Fig. 13c that the dimples are bigger and deeper, which also reflects better mechanical properties for the slices. This is because that, the ductile tensile fracture is characterized by numerous tear ridges, reflecting the material's ability to sustain the tensile load after microvoid coalescence has begun. Absence of the ridges indicates that the brittle specimens would fail soon after commencement of microvoid coalescence [42]. Mahoney et al. [43] also reported similar results for FSW of AA7075-T651 alloy and concluded that ductile behavior of tensile FSW joints was due to the presence of precipitate free zones at grain boundaries.

To further analyze the fracture characteristic of overall joints, the surface morphologies of the fractured specimens obtained by TC are shown in Fig. 14. Clearly, the failure surface is smooth, and the ductile dimpled fracture regions are found in Fig. 14a. The joint which fractures at the HAZ during the tensile tests is due to the precipitation evolution as discussed above. The samples failed at the HAZ show two kinds of dimples: the coarser primary particles (see Fig. 14b) and finer precipitated phase particles (see Fig. 14c, d). Sharma et al. [42] reported that the coarser primary particles which nucleated from the voids were rich in Mg and Zn elements, and the finer precipitated phase particles stemmed from the micro voids, which nucleated in the ligament between the primary voids due to the dispersoids. Similar results were found in FSW of AA6005 alloy by Nielsen et al. [44]. Therefore, the global mechanical properties of the joints welded by using the TC are significantly improved in this investigation.

4 Conclusions

In this investigation, four tools with different pin-tip profiles were designed to friction stir weld 20-mm-thick AA7075-T6 alloy plates. Microstructure, microhardness, and tensile properties of the bottom slices and overall joints were compared and discussed. It is concluded that

1. The dynamic recrystallized grains in the BNZs were significantly refined compared to those welded by TA. The average grain sizes estimated by EBSD were about 10.8, 7.7, 3.5, and 4.7 μm obtained by using TA, TB, TC, and TD, respectively. A similar trend of the grain sizes occurred in the middle of weld.
2. Finer and more dispersive precipitated phases in the BNZ were produced by using TC. Most of precipitated particles were examined as η phase by using XRD, and its content was the highest. Moreover, a higher density of dislocations was found. This BNZ hardness observably increased.
3. The bottom slices with superior strength and ductility were obtained in the case of TC. The ultimate tensile strength, yield strength, and elongation were the highest with compared to ones welded by other tools, which were 388 MPa, 315 MPa, and 7.9 %, respectively. This was attributed to finer grains, more HAGBs, more dispersive and higher content of precipitates, and optimum hardness distribution. Accordingly, the mechanical properties of the overall joints significantly improved.
4. The failure mechanism of the slices changed into a ductile fracture through using TC tool. The fracture morphologies of the overall joints exhibited a typical ductile fracture with a large amount of dimples and tearing edges, accounting for better strength and ductility.

Acknowledgments This work was supported by the National Natural Science Foundation of China (NSFC) (Nos. 51265043 and 51265042) and the Landed Plan of Science and Technology in Colleges and Universities of Jiangxi Province (No. KJLD12074).

References

1. Sharma C, Dwivedi DK, Kumar P (2013) Effect of post weld heat treatments on microstructure and mechanical properties of friction stir welded joints of Al-Zn-Mg alloy AA7039. *Mater Des* 43:134–143
2. Su JQ, Nelson TW, Mishra R, Mahoney M (2003) Microstructural investigation of friction stir welded 7050-T651 aluminium. *Acta Mater* 51:713–729
3. Bahemmat P, Haghpanahi M, BesharatiGivi M, Reshad Seighalani K (2012) Study on dissimilar friction stir butt welding of AA7075-O and AA2024-t4 considering the manufacturing limitation. *Int J Adv Manuf Technol* 59(9–12):939–953
4. Fu RD, Sun ZQ, Sun RC, Li Y, Liu HJ, Liu L (2011) Improvement of weld temperature distribution and mechanical properties of 7050 aluminum alloy butt joints by submerged friction stir welding. *Mater Des* 32:4825–4831
5. Fuller CB, Mahoney MW, Calabrese M, Miconi L (2010) Evolution of microstructure and mechanical properties in naturally aged 7050 and 7075 Al friction stir welds. *Mater Sci Eng A* 527:2233–2240
6. Balasubramanian V, Ravikiran V, Madhusudhan RG (2008) Effect of postweld aging treatment on fatigue behavior of pulsed current welded AA7075 aluminum alloy joints. *J Mater Eng Perform* 7: 224–233
7. Feng AH, Chen DL, Ma ZY (2010) Microstructure and cyclic deformation behavior of a friction-stir-welded 7075 Al alloy. *Metall Mater Trans A* 41:957–971
8. Singh R, Sharma C, Dwivedi D, Mehta N, Kumar P (2011) The microstructure and mechanical properties of friction stir welded Al-Zn-Mg alloy in as welded and heat treated conditions. *Mater Des* 32(2):682–687

9. Sivaraj P, Kanagarajan D, Balasubramanian V (2014) Effect of post-weld heat treatment on tensile properties and microstructure characteristics of friction stir welded armour grade AA7075-T651 aluminium alloy. *Def Technol Bus* 10(1):1–8
10. Mao YQ, Ke LM, Liu FC, Huang CP, Chen YH, Liu Q (2015) Effect of welding parameters on microstructure and mechanical properties of friction stir welded joints of 2060 aluminum lithium alloy. *Int J Adv Manuf Technol* 81(5):1419–1431
11. Mironov S, Masaki K, Sato YS, Kokawa H (2012) Relation between material flow and abnormal grain growth in friction-stir welds. *Scr Mater* 67:983–986
12. Krishnan KN (2002) On the formation of onion rings in friction stir welds. *Mater Sci Eng A* 327:246–251
13. Scialpi A, De Filippis LAC, Cavaliere P (2007) Influence of shoulder geometry on microstructure and mechanical properties of friction stir welded 6082 aluminum alloy. *Mater Des* 28:1124–1129
14. Fujii H, Cui L, Maeda M, Nogi K (2006) Effect of tool shape on mechanical properties and microstructure of friction stir welded aluminum alloys. *Mater Sci Eng A* 419:25–31
15. Zhou CZ, Yang XQ (2006) Effect of kissing bond on fatigue behavior of friction stir welds on Al 5083 alloy. *J Mater Sci* 41:2771–2777
16. Paglia CS, Buchheit RG (2008) A look in the corrosion of aluminum alloy friction stir welds. *Scr Mater* 58:383–387
17. Avettand Fenoel M, Taillard R (2015) Heterogeneity of the nugget microstructure in a thick 2050 Al friction-stirred weld. *Metall Mater Trans A* 46A:300–314
18. Canaday Clinton T, Moore Matthew A, Tang W, Reynolds AP (2013) Through thickness property variations in a thick plate AA7050 friction stir welded joint. *Mater Sci Eng A* 559:678–682
19. Srinivasa Rao T, Madhusudhan Reddy G, Koteswara Rao SR (2015) Microstructure and mechanical properties of friction stir welded AA7075T651 aluminum alloy thick plates. *Trans Nonferrous Metals Soc China* 25:1770–1778
20. Xu WF, Liu JH, Luan GH, Dong CL (2009) Temperature evolution, microstructure and mechanical properties of friction stir welded thick 2219-O aluminum alloy joints. *Mater Des* 30:1886–1893
21. Mishra RS, Ma ZY (2005) Friction stir welding and processing. *Mater Sci Eng R* 50:1–78
22. Nandan R, Deb Roy T, Bhadeshia HKDH (2008) Recent advances in friction stir welding-process, weldment structure and properties. *Prog Mater Sci* 53:980–1023
23. Liu H, Chen Y, Feng J (2006) Effect of zigzag line on the mechanical properties of friction stir welded joints of an Al-Cu alloy. *Scr Mater* 55:231–234
24. Thomas WM, Nicolash ED, Smith SD (2001) Friction stir welding-Tool developments. In: Das SK, Kaufman JG, Lienert TJ, editors. *Aluminium 2001 proceedings of the TMS 2001 aluminum automotive and joining session, TMS*; 213–224.
25. Zhang YN, Cao X, Larose S, Wanjara P (2012) Review of tools for friction stir welding and processing. *Can Metall Q* 51(3):250–261
26. Thomas WM, Nicholas ED (1997) Friction stir welding for the transportation industries. *Mater Des* 18:269–273
27. Elangovan K, Balasubramanian V (2008) Influences of tool pin profile and tool shoulder diameter on the formation of friction stir processing zone in AA6061 aluminum alloy. *Mater Des* 29:362–373
28. Dawood HI, Mohammed KS, Rahmat A, Uday MB (2015) Effect of small tool pin profiles on microstructures and mechanical properties of 6061 aluminum alloy by friction stir welding. *Trans Nonferrous Metals Soc China* 25:2856–2865
29. Khodaverdizadeh H, Heidarzadeh A, Saeid T (2013) Effect of tool pin profile on microstructure and mechanical properties of friction stir welded pure copper joints. *Mater Des* 45:265–270
30. Heidarzadeh A, Kazemi-Chooobi K, Hanifian H, Asadi P (2014) Microstructural evolution. In: Givi MKB, Asadi P (eds) *Advances in friction-stir welding and processing*. Woodhead Publishing, Cambridge, pp 65–140. doi:10.1533/9780857094551.65
31. Mao YQ, Ke LM, Liu FC, Liu Q, Huang CP, Xing L (2014) Effect of tool pin eccentricity on microstructure and mechanical properties in friction stir welded 7075 aluminum alloy thick plate. *Mater Des* 62:334–343
32. McNelley TR, Swaminathan S, Su JQ (2008) Recrystallization mechanisms during friction stir welding/processing of aluminum alloys. *Scr Mater* 58(5):349–354
33. Zhao YH, Zhu YT, Lavernia EJ (2010) Preparation of nanostructured materials having improved ductility. *Adv Eng Mater* 12:769–788
34. Chinh NQ, Szommer P, Horita Z, Langdon TG (2006) Experimental evidence for grain-boundary sliding in ultrafine-grained aluminum processed by severe plastic deformation. *Adv Mater* 18:34–39
35. Mao YQ, Ke LM, Liu FC, Chen YH, Xing L (2015) Investigations on temperature distribution, microstructure evolution and property variations along thickness in friction stir welded joints for thick AA7075-T6 plates. *Int J Adv Manuf Technol*. doi:10.1007/s00170-015-8182-z
36. Feng ZQ, Yang YQ, Huang B, Han M, Luo X, Ru JG (2010) Precipitation process along dislocations in Al–Cu–Mg alloy during artificial aging. *Mater Sci Eng A* 528:706–714
37. Feng AH, Chen DL, Ma ZY (2010) Microstructure and low-cycle fatigue of a friction-stir-welded 6061 aluminum alloy. *Metall Mater Trans A* 41:2626–2641
38. Mironov S, Masaki K, Sato YS, Kokawa H (2012) Relationship between material flow and abnormal grain growth in friction-stir welds. *Scr Mater* 67(12):983–986
39. Starink MJ, Deschamps A, Wang SC (2008) The strength of friction stir welded and friction stir processed aluminium alloys. *Scr Mater* 58:377–382
40. Hu ZL, Wang XS, Yuan SJ (2012) Quantitative investigation of the tensile plastic deformation characteristic and microstructure for friction stir welded 2024 aluminum alloy. *Mater Charact* 73:114–123
41. Sato YS, Urata M, Kokawa H, Ikeda K (2003) Hall–Petch relationship in friction stir welds of equal channel angular-pressed aluminum alloys. *Mater Sci Eng A* 354:298–305
42. Sharma C, Dwivedi DK, Kumar P (2013) Effect of welding parameters on microstructure and mechanical properties of friction stir welded joints of AA7039 aluminum alloy. *Mater Des* 36:379–390
43. Mahoney MW, Rhodes CG, Flintoff JG, Spurling RA, Bingel WH (1998) Properties of friction stir welded 7075 T651 aluminum. *Metall Mater Trans A* 29A:1955–1964
44. Nielsen KL, Pardoent T, Tvergaard V, de Meester B, Simar A (2010) Modelling of plastic flow localisation and damage development in friction stir welded 6005A aluminium alloy using physics based strain hardening law. *Int J Solids Struct* 47(18–19):2359–2370